Phosphonium-based polythiophene conjugated polyelectrolytes with different surfactant counterions: thermal properties, self-assembly and photovoltaic performances

Michèle Chevrier,[1,2] Jurgen Kesters,[3] Judith E. Houston,[4] Niko Van den Brande,[5] Sylvain Chambon,[6] Sébastien Richeter,[1] Bruno Van Mele,[5] Thomas Arnold,[7,8,9,10] Ahmad Mehdi,[1] Roberto Lazzaroni,[11] Philippe Dubois,[2] Rachel C. Evans,[12*] Wouter Maes,[3] Sébastien Clément[1*]

1. ICGM, Univ. Montpellier, CNRS, ENSCM, Montpellier, France.
2. Service des Matériaux Polymères et Composites (SMPC), Centre d'Innovation et de Recherche en Matériaux et Polymères (CIRMAP), Université de Mons - UMONS, Place du Parc 20, 7000 Mons, Belgium
3. UHasselt – Hasselt University, Institute for Materials Research (IMO), Design & Synthesis of Organic Semiconductors (DSOS), Agoralaan 1, 3590 Diepenbeek, Belgium
4. Jülich Centre for Neutron Science (JCNS) at the Heinz Maier-Leibnitz Zentrum (MLZ), Forschungszentrum Jülich GmbH, Lichtenbergstr. 1, 85748 Garching, Germany
5. Physical Chemistry and Polymer Science (FYSC), Vrije Universiteit Brussel (VUB), Pleinlaan 2, 1050 Brussels, Belgium
6. Univ. Bordeaux, IMS, CNRS, UMR 5218, Bordeaux INP, ENSCBP, F-33405 Talence, France
7. Diamond Light Source Ltd, Harwell Science and Innovation Campus, Didcot, OX11 0D11, UK
8. European Spallation Source ERIC, P.O Box 176, SE-221 00 Lund, Sweden
9. Department of Chemistry, University of Bath, Claverton Down, Bath, BA2 7AY, UK
10. ISIS Neutron and Muon Source, Rutherford Appleton Laboratory, Didcot, OX11 0QX, UK

11. Laboratory for Chemistry of Novel Materials, CIRMAP, University of Mons - UMONS, Place du Parc 20, 7000 Mons, Belgium

12. Department of Materials Science & Metallurgy, University of Cambridge, 27 Charles Babbage Road, Cambridge, CB3 0FS, UK

ABSTRACT

Phosphonium-based polythiophene conjugated polyelectrolytes (CPEs) with three different counterions (dodecylsulfate (DS), octylsulfate (OS) and perfluorooctylsulfonate (PFOS)) are synthesized to determine how the nature of the counterion affects the thermal properties, the self-assembly in thin films and the performance as cathode interfacial layer in polymer solar cells (PSCs). The counterion has a significant effect on the thermal properties of the CPEs, affecting both their glass transition and crystalline behavior. Grazing-incidence wide-angle X-ray scattering (GIWAXS) studies also indicate that changing the nature of the counterion influences the microstructural organization in thin films (face-on *vs*. edge-on orientation). The affinity of the CPEs with the underlying photoactive layer in PSCs is highly correlated with the counterion species. Finally, in addition to an increase of the power conversion efficiency of ~15% when using these CPEs as cathode interfacial layers in PSCs, a higher device stability is noted, as compared to a reference device with a calcium interlayer.

KEYWORDS:

Conjugated polyelectrolytes, surfactant counteranion, self-assembly, thin films, cathode interlayers, organic solar cells

1. Introduction

Conjugated polyelectrolytes (CPEs) are polymers with a π-delocalized backbone bearing ionic side chain groups.[1] CPEs combine the physicochemical properties of polyelectrolytes, which are dependent on complex long-range electrostatic interactions with the optical and electronic properties of organic semiconducting polymers, which are closely linked to the chain conformation and interchain interactions.[1] The presence of pendant substituents with ionic functionalities allow their dissolution in highly polar solvents, including water, and their

interaction with other ionic species such as metal ions, molecular ions, polyelectrolytes, proteins and DNA through electrostatic interactions.[23] Thus, combining the intrinsic light-harvesting properties of the conjugated polymer backbone with the solubility in aqueous media has opened the door to the use of those materials as optical platforms for the detection of biological targets with increased sensitivity compared to small molecules.[4-7] Besides chemo- and biosensing, CPEs also showed great potential for application in organic optoelectronic devices such as light-emitting diodes,[8-13]organic electrochemical transistors[14-18] and organic photovoltaic devices (OPVs).[12, 13, 19, 20] Indeed, their solubility in highly polar solvents offers the opportunity to fabricate multilayer devices without interface mixing by depositing different layers from orthogonal solvents.[13, 20, 21] In addition, the presence of the ionic side groups has been found to induce the formation of an interfacial dipole, leading to a reduced work function (W_F) of the metal electrodes and thus, improved charge collection and performance.[22-25]

Optoelectronic devices are generally fabricated through solution processing. Due to their inherent amphiphilic nature, CPEs tends to self-assemble into aggregates with a conducting core (hydrophobic conjugated backbone) and an insulating shell (hydrophilic ionic pendant groups) which nucleate and drive the film morphology.[26-28] As such, large insulating domains between conduction pathways (i.e., π–π interactions) are expected from this self-assembly, which are detrimental for device performance. Since the device performance depends both on the intrinsically linked optoelectronic properties and nanoscale morphology of the polymer,[29, 30] determining the parameters influencing the CPE thin film morphology and its interdependent optoelectronic properties is paramount for achieving high-performance organic optoelectronic devices.

Among the structural parameters that might affect the self-assembly and the optoelectronic properties, the nature of the charge-compensating counterions has been identified as a possible lever to control such properties.[31-33] Indeed, Mc Cullough and coworkers have observed the strong dependence of the absorption spectra of polythiophene-based CPEs on the counterion nature, in particular its size.[34] Larger counterions prevent polyionic main chains from getting into contact with each other by increasing the average interchain distance, which reduces aggregation of polyions and fluorescence self-quenching.[31-33, 35] Similarly, the exchange of the native counterion by an ionic surfactant has also been proven to break-up CPE aggregates, leading to the formation of well-organized structures across multiple length scales.[27, 36-42] The type of charge-compensating counterions can also significantly influence the electronic properties of CPEs.[32, 35, 43, 44] Cao and coworkers have described how the type of counterion

species can fine-tune the self-doping behavior of n-type CPEs as well as the charge transport.[35] In addition, the properties of the interfaces in organic electronic devices can be fine-tuned by changing the type of counteranions in CPE deposited on the electrode generally leading to a decrease of the W_F of the electrodes, a better charge extraction and orders of magnitude changes in device performance.[35, 45, 46]

Herein, we examine a series of phosphonium-based polythiophenes incorporating a variety of charge-compensating counterions (X^-), namely dodecyl sulfate (DS), octyl sulfate (OS) and perfluorooctanesulfonate (PFOS) (**P3HTPMe$_3$,X**, Scheme 1). The study of their thermal properties reveals different degrees of crystallinity depending on the nature of the counterion. The self-assembly of the different CPEs in thin films is also investigated using grazing-incidence wide-angle X-ray Scattering (GIWAXS). Cationic polythiophene-based CPEs have been found to be interesting materials for interfacial engineering in polymer solar cells (PSCs) enabling improved charge extraction and thus, power conversion efficiency (PCE).[19, 21, 47-49] Based on these results, the performance and the device stability in air of PSCs incorporating this series of CPEs with different counterions as cathodic interfacial layers have been determined.

2. Materials and methods

2.1. Materials

All reactions were carried out under argon using standard high-vacuum and Schlenk techniques. Dry THF was obtained by the solvent purification system PureSolve MD5 from Innovative Technology. Perfluorooctanesulfonic acid potassium salt (PFOSK) (98%) and sodium octyl sulfate (SOS) (95%) were purchased from Sigma Aldrich and used as received. **P3HTPMe$_3$** and **P3HTPMe$_3$,DS** were prepared according to previously reported procedures.[21, 50]

2.2. Characterization methods

^{1}H, ^{13}C{^{1}H}, ^{31}P{^{1}H} and ^{19}F NMR spectra were acquired with Bruker Avance 300 MHz and 600 MHz spectrometers, using the solvent as the chemical shift standard. All chemical shifts and coupling constants are reported in ppm and Hz, respectively.

Number-averaged (M_n) and weight-averaged (M_w) molecular weights and the molecular weight distribution (Đ) of **P3HTBr** were measured using size exclusion chromatography (SEC) on a Polymer Laboratories liquid chromatograph equipped with a PL-DG802 degasser, an isocratic HPLC pump LC 1120 (flow rate of 1 mL min^{-1}), a Marathon

autosampler (loop volume of 200 mL, solution concentration of 1 mg mL^{-1}), a PL-DRI refractive index detector, and three columns: a PL gel 10 mm guard column and two PL gel Mixed-B 10 mm columns (linear columns for the separation of molecular weight polystyrene standards ranging from 500 to 10^6 Da). The eluent used was THF at a flow rate of 1 mL min^{-1} at 35 °C. Polystyrene standards were used to calibrate the SEC. XPS analyses were performed using an Omicron Argus X-ray photoelectron spectrometer with a monochromated AlK_α radiation source ($h\nu$ = 1486.6 eV) with a 300 W electron beam power. The emission of photoelectrons from the sample was analyzed at a takeoff angle of 90° under ultra-high vacuum conditions (≤ 10^{-10} Torr). The spectra were obtained with a 100 eV pass energy for the survey scan and 20 eV pass energy for the F1s, C1s, O1s, N1s, S2p and P2p regions. All binding energies were calibrated against the C1s peak at 284.6 eV. The element peak intensities were corrected by Scofield factors.[51, 52] The peak areas were determined after subtraction of a linear background. The spectra were fitted using Casa XPS v.2.3.15 software (Casa Software Ldt, UK) and applying a Gaussian/Lorentzian ratio G/L equal to 70/30.[51]

The electrochemical measurements were performed with an EcoChemie Autolab PGSTAT 30 Potentiostat using a three-electrode microcell with a platinum wire working electrode, a platinum wire counter electrode and an anhydrous $Ag/AgNO_3$ reference electrode ($Ag/0.1\ M\ NBu_4PF_6$ in MeCN containing 0.01 M $AgNO_3$). The CPEs were analysed in solution in anhydrous acetonitrile containing 0.1 M NBu_4PF_6. The electrolyte solution was degassed with Ar prior to each measurement. To prevent air from entering the system, a curtain of Ar was maintained during the differential pulse voltammetry (DPV) experiments. For the conversion of V to eV, the onset potentials of the first oxidation/reduction peaks were used and referenced to ferrocene/ferrocenium, which has an ionization potential of −4.98 eV *vs.* vacuum. This correction factor is based on a value of 0.31 eV for Fc/Fc^+ *vs.* SCE[53] and a value of 4.68 eV for SCE *vs.* vacuum[54] : $E_{HOMO/LUMO}$ (eV) = $-4.98 - E_{onset\ ox/red}^{Ag/AgNO3}$ (V) + $E_{onset\ Fc/Fc+}^{Ag/AgNO3}$ (V).

Thermal analyses were performed using a TA Instruments rapid heat-cool calorimeter (RHC), equipped with liquid nitrogen cooling and specifically designed for operation at high scanning rate.[55] Helium (10 mL min^{-1}) was used as a purge gas. Before each experiment, the thermal history of the materials was erased by an initial heating cycle, ensuring the reproducibility of the observed transitions. It is worthwhile to mention that no solvent effects were seen in this initial heating, with the exception of a slight effect for **P3HTPMe$_3$,PFOS**, most likely caused by the presence of some residual solvent due to the preparation method. The

measurements were performed by cooling at 500 K min^{-1} or 20 K min^{-1}, followed by heating at 500 K min^{-1} used for data interpretation.

Atomic force microscopy (AFM) measurements were performed using an Asylum Research MFP-3D™ instrument mounted on an anti-vibration plinth, in the tapping mode at room temperature under ambient conditions. Higher resolution AFM measurements were performed using diamond tips on silicon cantilevers, which were a kind gift from Adama Innovations. The silicon cantilevers had a spring constant of ~110 nN nm^{-1} and resonance frequency of ~240 kHz. All raw AFM images were analyzed using the Gwyddion 2.31 software.

Contact Potential Difference (CPD) was determined using a Kelvin Probe set up from Besocke Delta Phi. A methanol solution containing the conjugated polyelectrolyte (C =1 mg mL^{-1}) was prepared in nitrogen-filled glove box and stirred at room temperature for 24h. ITO-coated glass was cleaned using successive baths of Hellmanex, deionized water and isopropanol under sonication. 80 nm of silver (Ag) was deposited on ITO-coated glass by thermal evaporation under high vacuum (P = 2.10^{-6} mbar). Conjugated polyelectrolyte was deposited on the electrode (ITO and Ag) by spin-coating at 1000 rpm for 60s. The CPD of the different samples was measured subsequently and the Work Function (W_F) was estimated using freshly cleaved highly ordered pyrolytic graphite (HOPG) as a reference (4.65 eV).

GIWAXS measurements were performed on beamline I07, Diamond Light Source, U.K.[56] The X-ray beam energy was E = 10 keV (wavelength, λ = 1.24 Å) and the beam size was ~ 100 × 200 μm (v × h, full-width half-maximum, FWHM) with an approximately Gaussian intensity profile. An incident angle of αi = 0.4° (>2 × αc, the critical angle) was used, as this allows for complete illumination of the films with minimal substrate-reflected beam which could complicate analysis. The data were collected on a Pilatus P2M detector (DECTRIS) using a sample-to-detector distance of ~237 mm, calibrated with silver behenate, giving an angular coverage of ~30° and a q-range of 0.1-3.5 $Å^{-1}$. **P3HTPMe$_3$,X** samples for GIWAXS were prepared by mixing 10 mg mL^{-1} solutions of **P3HTPMe$_3$** with 10 mg mL^{-1} solutions of surfactant to obtain the desired 1:1 charge ratio, with a *total* concentration of 10 mg mL^{-1}. The compositions of **P3HTPMe$_3$**-surfactant mixtures are given in the ESI (Table S2 in the Supporting Information). Solutions of **P3HTPMe$_3$,X** CPEs mixed with different counterions were spin-coated onto silicon wafers from 10 mg mL^{-1} methanolic solutions, resulting in films that were 70-80 nm thick. The samples were enclosed in a helium-filled

chamber to reduce beam damage and background scattering and mounted on a hexapod to allow alignment. A fast shutter prevented unintended exposure to X-rays with extremely short exposure times of 1 second. The data were reduced using the data reduction and analysis software Data Analysis WorkbeNch (DAWN) and beamline scripts.[57] DAWN was also used to identify peak positions and widths, which have been directly related to the morphology.

2.3. OPV device fabrication and characterization

Bulk heterojunction polymer solar cells were fabricated using the traditional architecture glass/ITO/PEDOT:PSS/PCDTBT:$PC_{71}BM$/**P3HTPMe$_3$,X** (or Ca)/Al. The PCDTBT donor polymer (M_n = 79 kDa, Đ = 2.4) and $PC_{71}BM$ (Figure S12, SI) were obtained from SolarisChem and Solenne, respectively. Prior to processing, the indium tin oxide (ITO; Kintec, 100 nm, 20 Ohm sq^{-1}) coated glass substrates were thoroughly cleaned using soap, demineralized water, acetone, isopropanol and a UV/O_3 treatment. PEDOT:PSS (poly(3,4-ethylenedioxythiophene):poly(styrenesulfonic acid); Heraeus Clevios) was then deposited via spin-coating to obtain a layer thickness of ~30 nm. Further processing was continued in a nitrogen-filled glovebox (O_2/H_2O < 0.1 ppm), initiated by thermal treatment for 15 min at 130 °C to remove any residual water. The photoactive layer blend PCDTBT:$PC_{71}BM$ was then spin-coated in a 1:4 ratio with a total concentration of 20 mg mL^{-1} from an *ortho*-dichlorobenzene solution. For the reference device without the CPE interlayer, Ca and Al electrodes were deposited with a thickness of ~30 and ~80 nm, respectively. For devices employing the interlayer materials, the CPEs were spin-coated from methanol as a processing solvent in different concentrations (0.25, 0.5 and 1 mg mL^{-1}) to optimize the solar cell parameters. Device fabrication was then completed by the deposition of an Al layer as the top electrode. The I-V characteristics were measured using a Newport class A solar simulator (model 91195A), calibrated with a silicon solar cell to give an AM 1.5G spectrum. All data shown in this work are average values over 4–8 cells. For the stability measurements, new devices were prepared with the optimized CPE concentrations and these solar cells were subjected to ambient air (in the dark) for 40, 80 and 120 min. I-V measurements were subsequently performed in a nitrogen atmosphere. AFM experiments on the solar cell devices were performed with a JPK NanoWizard 3 AFM (JPK Instruments AG, Berlin, Germany) using AC mode in air. Silicon ACTA-50 tips from AppNano with cantilever length ~125 mm, spring constant ~40 N/m and a resonance frequency ~300 kHz were used. The scan angle, set point height, gain values and scan rate were adjusted according to the calibration of the AFM tip.

2.4.Polymer synthesis

General procedure for bromide counterion exchange by octyl sulfate (OS). **P3HTPMe$_3$** (0.100 g, 0.31 mmol) was dissolved in demineralized water (20 mL) and a solution of sodium octyl sulfate (0.720 g, 3.11 mmol) in demineralized water (10 mL) was added dropwise. The solution was stirred at room temperature overnight and then, poured into acetone (600 mL). The resultant black solid was filtered off, washed with acetone and dried under vacuum. Yield: 81% (0.140 g). ^{1}H NMR (CD_3OD): δ = 0.90 (t, CH_3, 3H, $^3J_{H–H}$ = 7.0 Hz), 1.25-1.36 (m, 8H), 1.36-1.44 (m, 2H), 1.52-1.73 (m, 10H), 1.74-1.84 (m, 2H), 1.90 (d, 9H, $(CH_3)P$, $^2J_{P–H}$ = 14.5 Hz), 2.22-2.34 (m, 2H), 2.92 (br. t, 2H, $^3J_{H-H}$ = 7.8 Hz), 3.99 (t, 2H, CH_2–O–SO_3, $^3J_{H–H}$ = 6.6 Hz), 7.14 (s, 1H, Th) ppm. ^{13}C{^{1}H} NMR (CD_3OD): δ = 8.8 (d, $^1J_{P–C}$ = 55.0 Hz), 15.4, 23.3, 24.6, 24.8, 25.1, 30.8, 31.3, 31.4, 32.3, 32.4, 32.5, 33.9, 69.9, 131.1, 132.6, 135.8, 142.3 ppm. ^{31}P{^{1}H} NMR (CD_3OD): δ = 27.2 ppm. UV/Vis (MeOH): λ_{max} = 445 nm.

General procedure for bromide counterion exchange by perfluoroctanesulfonate (PFOS). **P3HTPMe$_3$** (0.100 g, 0.31 mmol) was dissolved in methanol (20 mL) and a solution of perfluorooctanesulfonic acid potassium salt (PFOSK) (1.000 g, 1.86 mmol) in a 1:1 methanol/acetone mixture (20 mL) was added dropwise. The solution was stirred at room temperature overnight and then poured into diethyl ether (600 mL) to precipitate the polymer. After filtration, the residue was suspended in water (500 mL) and stirred at 50 °C for 24 h to remove the excess of PFOSK. The polymer was then isolated by filtration, washed with water (3 × 30 mL) and diethyl ether (3 × 30 mL) and dried under vacuum, leading to a red solid. Yield: 76% (0.229 g). ^{1}H NMR (acetone-d_6): δ = 1.55-1.63 (m, 4H), 1.74-1.81 (m, 4H), 2.03 (d, 9H, $(CH_3)P$, $^2J_{P–H}$ = 14.7 Hz), 2.42-2.48 (m, 2H), 2.92 (br. t, 2H, $^3J_{H-H}$ = 7.8 Hz), 7.23 (s, 1H, Th) ppm. ^{19}F NMR (acetone-d_6): δ = -72.6, -81.7, -115.1, -120.9, -122.7, -123.2, -126.7 ppm. ^{31}P{^{1}H} NMR (acetone-d_6): δ = 27.7 ppm. UV/Vis (MeOH): λ_{max} = 447 nm.

3. Results and discussion

3.1. Polymer synthesis and characterization

The phosphonium-substituted polythiophene polyelectrolyte starting material was synthesized according to a previously reported procedure.[50] Briefly, Kumada Catalyst-Transfer Condensative Polymerization (KCTCP) was first used to generate the neutral bromohexyl-functionalized precursor, **P3HTBr** (M_n = 13600 g mol^{-1}, Đ = 1.36). Post-polymerization reaction with trimethylphosphine introduced the phosphonium cationic moiety, yielding

P3HTPMe$_3$. As a final modification, the counterion exchange was carried out by adding an excess of salt from the counterion of interest into a **P3HTPMe$_3$** solution while vigorously stirring (Scheme 1).

After precipitation, the resulting solid was filtered off on a cellulose membrane, washed and dried in vacuo affording **P3HTPMe$_3$,X** (where X = octyl sulfate (OS), dodecyl sulfate (DS)[21] or perfluorooctanesulfonate (PFOS)). Ion exchange was confirmed by ^{1}H NMR spectroscopy and X-ray photoelectron spectroscopy (XPS). The signals at 2.92 and 3.99 ppm in the ^{1}H NMR spectrum of **P3HTPMe$_3$,OS**, assigned to the methylene groups linked to the thiophene ring and the methylene groups adjacent to the sulfate in the OS anion, respectively allowed to determine the molar ratio between the cationic polythiophene and the OS anionic moieties (Fig. S1 in the Supporting Information). By integrating these two signals, the molar ratio between **P3HTPMe$_3$** and OS was found to be very close to 1:1, as expected. The presence of the PFOS counterion in the **P3HTPMe$_3$,PFOS** CPE was evidenced using ^{19}F NMR spectroscopy, where signals at -72.6, -81.7 and between -115 and -127 ppm were observed (Fig. S5 in the Supporting Information). In the XPS spectra of the CPEs following the exchange of Br^- with different anions (Fig. S7-S9 in the Supporting Information), the Br3d peak at 68 eV was no longer observed, indicating that the counterion exchange occurred quantitatively. The frontier orbital energy levels of the three **P3HTPMe$_3$,X** were determined by differential pulse voltammetry (DPV). The onset oxidation potentials were estimated to be 0.12, 0.27 and 0.30 V (*vs*. Fc/Fc$^+$) for **P3HTPMe$_3$,DS**, **P3HTPMe$_3$,PFOS** and **P3HTPMe$_3$,OS**, respectively. From these values, the highest occupied molecular orbital (HOMO) energy levels were calculated as -5.01, -5.17 and -5.20 eV for **P3HTPMe$_3$,DS**, **P3HTPMe$_3$,PFOS** and **P3HTPMe$_3$,OS**, respectively (Table S1 in the Supporting Information). Similarly, the nature of the counterions also has little effect on the lowest occupied molecular orbital (LUMO) energy levels with values of -2.99 eV, -2.98 eV and -2.96 eV for **P3HTPMe$_3$,DS**, **P3HTPMe$_3$,PFOS** and **P3HTPMe$_3$,OS**, respectively, which were determined from the onset reduction potentials.

3.2. Thermal properties

The thermal behavior of the synthesized **P3HTPMe$_3$,X** materials was studied by rapid heat-cool calorimetry (RHC) (Fig. 1). Both a rapid cooling rate at 500 K min^{-1} and a more conventional cooling rate at 20 K min^{-1} were used. **P3HTPMe$_3$,PFOS** was found to be completely amorphous, exhibiting a glass transition (T_g) at about 95 °C. We note that this

material remained fully amorphous when the cooling rate was lowered to 20 K min^{-1}. In contrast, we have reported in a previous study that **P3HTPMe$_3$,DS** exhibits semi-crystalline behavior,[21] with a T_g at about 70 °C, followed by cold crystallization when cooled at 500 K min^{-1}. The enthalpic value of the cold crystallization equals that of the subsequent melting endotherm, proving the fully amorphous nature of this material after a 500 K min^{-1} cooling. After cooling at 20 K min^{-1}, a clear double melting peak was observed with maxima at 152 and 176 °C, and a combined melting enthalpy (ΔH_m) of 18.9 J g^{-1}. **P3HTPMe$_3$,OS** is also a semi-crystalline material, a higher degree of crystallinity, as a higher melting enthalpy was observed and no T_g could be detected. As in **P3HTPMe$_3$,DS**, a double melting peak is observed after 20 K min^{-1} cooling, with maxima at 179 and 220 °C, yielding a total ΔH_m of 26.7 J g^{-1}. The melting peak at 179 °C can be clearly seen even after 500 K min^{-1} cooling, indicating that **P3HTPMe$_3$,OS** crystallizes more rapidly than **P3HTPMe$_3$,DS**. It seems that the materials with the chemically similar DS and OS counterions show comparable behaviors, with the OS counterion leading to a higher crystallization rate and a more crystalline material. If the aliphatic chains in the OS counterion are fully fluorinated, the distorted *trans* conformation of the PFOS counterion seemingly prevents crystallization and leads to the completely amorphous **P3HTPMe$_3$,PFOS** material.

3.3. Microstructural organization in the thin polymer films

GIWAXS was used to probe the role of the counterion on the microstructural organization of thin films of **P3HTPMe$_3$** and **P3HTPMe$_3$,X**. Information on the relative crystallinity, polymer orientation and coherence length in thin films is straightforward to extract from 2D GIWAXS scattering patterns *via* the area, position and full-width at half maximum (FWHM) of the diffraction peaks.[58] X-rays are applied at an incident angle (α_i) above the critical angle (α_c) of the polymer films (~0.13°) and the silicon substrate (~0.18°) to penetrate the entire thickness of the polymer film (~70-80 nm), as well as a portion of the silicon substrate, to allow for better contrast of the diffraction features, while suppressing the effect of the reflected spot. Critical angles were calculated from the material scattering length densities (see Supporting Information). Figures 2a-d show the GIWAXS patterns for pristine **P3HTPMe$_3$**, **P3HTPMe$_3$,OS**, **P3HTPMe$_3$,PFOS** and **P3HTPMe$_3$,DS** films. The 2D GIWAXS patterns for all four samples exhibit distinct lamellar packing diffractions (denoted as (*h00*)) in the out-of-plane direction.[59] This crystal spacing suggests that the **P3HTPMe$_3$,X** CPE chains predominantly stack edge-on to the silicon substrate (Fig. 3).[59] The corresponding

line cuts along the out-of-plane (q_z, perpendicular to the substrate) and in-plane (q_{xy}, parallel to the substrate) directions are shown in Figures 2e and 2f, respectively.

For the pristine polymer, **P3HTPMe$_3$** (Fig. 2a), an intense (*100*) reflection centered at q_z = 2.5 nm^{-1} is observed. This correlates to a lamellar spacing between the CPE backbones and across the alkyl side chains of 2.56 nm (see Fig. 3a), which is significantly larger than the crystal spacing of poly(3-hexylthiophene) (P3HT) (1.64 nm).[60] A weak, broad reflection is also observed along the in-plane direction at q_{xy} = ~13.5 nm^{-1} (denoted as (*010*)). This peak results from π-π stacking between the CPE backbones and corresponds to a π-π distance of 0.47 nm. The position of the original (*100*) peaks in the out-of-plane direction of pristine **P3HTPMe$_3$** alters slightly upon exchange of the bromide counterions with PFOS, OS and DS, resulting in reduced lamellar spacings of 2.51, 2.42 and 2.51 nm, respectively (highlighted with red asterisks in Fig. 2e). However, the CPEs with hydrogenated counterions also exhibit a second set of (*h00*) peaks in the out-of-plane direction at slightly lower *q* (highlighted with blue asterisks in Fig. 2e). These peaks correspond to larger lamellar spacings of 2.86 and 2.73 nm for **P3HTPMe$_3$,OS** and **P3HTPMe$_3$,DS**, respectively. Furthermore, the (*100*) peak for **P3HTPMe$_3$,DS** extends into the in-plane direction (ring peak in Figure 2d). This suggests the coexistence of both edge-on and face-on orientations and may explain why two distinctive lamellar stacking peaks (blue and red asterisks) are observed for this compound. The position of the (010) peaks in the in-plane direction and thus, the π-π stacking distances, change slightly for **P3HTPMe$_3$,OS** and **P3HTPMe$_3$,DS** to 0.42 and 0.41 nm, respectively. In contrast, the π-π stacking distance in **P3HTPMe$_3$,PFOS** increases to 0.52 nm and, thus, PFOS is the only counterion to cause a reduction in packing of the CPE chains.

The extent of preferential orientation in the CPE films was further investigated by performing radial and azimuthal integrations of the 2D GIWAXS scattering patterns, as shown in Figure S10 in the Supporting Information). The azimuthal integrations for each of the CPEs around q_{xy} = 0 nm^{-1} show narrow peaks at -90°, which highlight the preferential orientation of the CPEs in the out-of-plane direction. The widths of these bands, and therefore, preferential orientation, decrease in the order **P3HTPMe$_3$** > **P3HTPMe$_3$,OS** > **P3HTPMe$_3$,PFOS** >> **P3HTPMe$_3$,DS**. The lack of orientation in the film of **P3HTPMe$_3$,DS** is clearly shown by the extremely diffuse peaks in the azimuthal integration.

The broadening of the diffraction peaks provides further information about the nature of the ordered regions within the **P3HTPMe$_3$,X** films. Peak broadening occurs due to fluctuation of the lattice spacing about a mean value, the so-called paracrystalline disorder.[61] The

paracrystallinity disorder parameter, *g*, can be determined from the in-plane π-π stacking reflections using:[61]

$$g = \sqrt{\frac{\Delta q}{2\pi q_0}}$$

where Δq is the FWHM of a Bragg diffraction peak and q_0 is the peak center. The larger the value of *g*, the greater the disorder.

The lamellar spacings, π-π stacking distances and *g* values for thin films of **P3HTPMe$_3$,X** are summarized in Fig. 3b. For pure **P3HTPMe$_3$** and **P3HTPMe$_3$,OS**, the (010) peaks at q = ~14.0 nm^{-1} are extremely weak and broad, giving large *g* values of 19-20%, which suggest a high degree of paracrystallinity disorder. For **P3HTPMe$_3$,PFOS** the (010) peak becomes slightly more intense although the paracrystallinity remains large at g = ~19%. In contrast, **P3HTPMe$_3$,DS** is significantly more ordered with g = ~14%. However, it should be noted that even this lower value remains significantly larger than that of thermally-annealed **P3HT** (g = 6-8%).[29]

These results seem to contrast with those obtained above from RHC studies where **P3HTPMe$_3$,OS** exhibits a higher degree of crystallinity than **P3HTPMe$_3$,DS**. However, since the CPE thin films are prepared from MeOH solutions, whereas the CPE powders are precipitated from acetone, different solution phase-structures and thus, a different degree of crystallinity may be expected for the powders and thin films as applied for the RHC and GIWAXS studies, respectively. This difference in the microstructural organization of the thin films of the CPEs depending on the nature of the counterion is also reflected in the morphology of the deposited CPE films. Indeed, while the morphology of the thin film of **P3HTPMe$_3$,OS** on a silicon wafer is largely featureless, the AFM images of **P3HTPMe$_3$,PFOS** and **P3HTPMe$_3$,DS** show large globular aggregates (Figure S11 in the Supporting Information).

Preferential face-on orientation and reduced π-π distances are favorable for vertical charge transport and charge carrier mobility.[62-64] The shorter π-π stacking distances imply stronger π-interactions between neighboring CPE chains.[65] Therefore, while P3HT-like chains typically lie perpendicular to the substrate,[66, 67] **P3HTPMe$_3$,DS** appears to have edge-on chains coexisting with face-on packing. In contrast, **P3HTPMe$_3$,PFOS** is seemingly amorphous in the RHC studies and has a relatively large *g* and significantly larger π-π stacking distance compared to the other CPE thin films.

3.4. Photovoltaic properties

The behavior of the **P3HTPMe$_3$,X** materials as cathode interlayers was then analyzed by fabricating bulk heterojunction (BHJ) PSCs with a conventional architecture (glass/ITO/PEDOT:PSS/PCDTBT:PC$_{71}$BM/CPE (or Ca)/Al). The chemical structures of the photoactive layer components are shown in Figure S12 in the Supporting Information. The photoactive layer was deposited from *ortho*-dichlorobenzene in a 1:4 ratio with PC$_{71}$BM, with a total concentration of 20 mg mL^{-1}. The CPE interlayers were then spin-coated directly on top of the photoactive layer from methanol solutions in various concentrations (0.25, 0.5 and 1 mg mL^{-1}) to determine at which concentration the various CPE interlayers should be deposited to produce the best device performance. As indicated in Table 1 and Figure 4, the incorporation of the **P3HTPMe$_3$,X** interlayers led to an improvement of all the device parameters (V_{OC}, J_{SC}, FF) and thus, in an increase in the PCE by ~15% as compared to the reference device with a calcium interlayer, in line with previous investigations on similar CPE interlayers.[21, 25, 47, 49] Nevertheless, similar PCEs are noticed regardless of the type of counterions.

Kelvin probe experiments were performed to study the work function (W_F) changes of the metal electrode in the presence of the CPE interlayer. Due to easy oxidation of Al in the atmospheric environment, we used Ag and ITO electrodes in replacement of the Al electrodes to measure the W_F change. The results of the Kelvin probe experiments indicate that the DS and OS counterions lead to a significant decrease of the W_F of the bare Ag (5.01 eV) and ITO (5.33 eV) electrodes to 4.23 eV (Ag) and 4.78 eV (ITO) for **P3HTPMe$_3$,DS**, and 4.15 eV (Ag) and 4.54 eV (ITO) for **P3HTPMe$_3$,OS.** Since it has been previously shown that CPEs lower the W_F of Ag and Al,[23, 68] it is reasonable to assume that the W_F of the Al electrodes used in our solar cell devices containing either **P3HTPMe$_3$,OS** and **P3HTPMe$_3$,DS** cathode interlayers will also be lowered. In the case of **P3HTPMe$_3$,PFOS**, no clear change is observed on the W_F of the bare Ag and ITO electrodes as 5.04 eV and 5.28 eV where measured for Ag/**P3HTPMe$_3$,PFOS** and ITO/**P3HTPMe$_3$,PFOS** respectively. Since reduced W_F of the electrodes is known to provide a better energy alignment between metal electrode and active layer which results in an enhancement of open-circuit voltage (V_{OC}) in devices,[69, 70] the weak effect of PFOS counterion on the W_F contrasts with the increased (V_{OC}) noted for **P3HTPMe$_3$,PFOS**-based devices. This result may suggest that the orientation of the interfacial dipole differs according to the nature of the substrate (photoactive layer *vs*. bare electrode) leading for **P3HTPMe$_3$,PFOS** to a reduced W_F when deposited on the photoactive layer while when deposited on the bare electrode, no effect is observed.

To investigate the morphology of the deposited CPE films on top of the PCDTBT:$PC_{71}BM$ active layers, AFM images were recorded for all CPE concentrations shown in Table 1. As demonstrated in Figure 5, the **P3HTPMe$_3$,X** CPEs do not completely cover the active layer surface and they exhibit strong differences in their deposition pattern depending on the nature of the counterion. Indeed, while **P3HTPMe$_3$,DS** and **P3HTPMe$_3$,PFOS** show reasonably good affinity for deposition on top of the photoactive layer, strong "dewetting" is observed for **P3HTPMe$_3$,OS**, with globular heights up to ~20 nm. However, this improved affinity does not seem to have a major influence on the final performance, since the PCEs for all the devices are very similar. Although this observation might be somewhat surprising, it is in line with previous studies on similar polythiophene CPEs,[21, 25, 47, 49, 71] in which it was shown that it is very difficult to pinpoint specific structural requirements for CPE materials. The introduction of ionic moieties induces the formation of interfacial dipoles (i.e. capacitive double layer), enhancing charge collection, while at the same time diminishing the affinity of the interlayer material for the active layer, and the increase in efficiency is dependent on the complex interplay of these two phenomena.

Finally, the stability in air of the BHJ-PSCs with **P3HTPMe$_3$,X** as the interfacial layer was also investigated. New devices were prepared with the optimized CPE concentrations and these were subjected to ambient air (in the dark) for 40, 80 and 120 min. *I-V* measurements were subsequently performed in a nitrogen atmosphere to avoid additional photo-oxidation processes. As can be observed from Figure 6 and Table S1, the reference device employing Ca as the interfacial layer degrades very quickly, with the initial PCE of 4.08% decaying rapidly to 0.55% after 40 min in air, before decreasing further to an average value of 0.13% after two hours. This very poor device stability can be attributed to the high reactivity of Ca with oxygen.[72] Although these polythiophene-based CPEs are good alternatives to Ca as interlayer materials with respect to their electronic properties, rapid degradation of the devices may still be observed under air and moisture (if non-encapsulated) when using them as the cathode interlayer. Indeed, **P3HTPMe$_3$,OS** exhibits serious air degradation, which is even faster than observed for the Ca/Al reference device. In contrast, all other devices employing CPE interlayers outlast the reference device, with the best device being that based on **P3HTPMe$_3$,DS**, mainly due to a better retention of the V_{oc}. It should also be noted that the devices with the more stable FFs are those with a more complete active layer coverage (Figure 2) (**P3HTPMe$_3$,PFOS** and **P3HTPMe$_3$,DS**), which could suggest more stable interfacial properties.

4. Conclusions

Three conjugated polyelectrolytes with identical polythiophene backbones and phosphonium side groups, but different charge-compensating ions, were synthesized. Changing the nature of the counterions drastically affects the glass transition temperature as well as the crystallinity of the materials. **P3HTPMe$_3$,PFOS** is completely amorphous, whereas **P3HTPMe$_3$,OS** and **P3HTPMe$_3$,DS** exhibit a semi-crystalline behavior. GIWAXS studies also indicate that the microstructural organization of thin polymer films is dependent on the nature of the counterion species. While **P3HTPMe3,DS** and **P3HTPMe$_3$,OS** exhibit shortened π-π stacking distances, the PFOS counterion causes a reduction in packing distance of the CPE chains. In addition, the coexistence of both edge-on and face-on orientations is also noticed for **P3HTPMe$_3$,DS**. Although AFM and Kelvin probe studies revealed different adhesion coverage efficiencies and work function changes depending on the nature of the counterion species, this does not lead to significant differences in their photovoltaic performance as cathode interfacial layers. To explain this behavior, a delicate balance between a wide variety of factors such as the material's affinity with the underlying photoactive layer, the ability to create a stable capacitive double layer[47] or the molecular ordering in thin films may be considered. Finally, some of these CPEs cathode interlayers lead to higher device stability in air in comparison with the reference device with a calcium interlayer, highlighting their potential for the fabrication of stable and highly performant polymer solar cells.

5. Acknowledgements

This work was supported by the CNRS and the Université de Montpellier. This work was also supported in part by the Science Foundation Ireland under Grant No. 12/IP/1608. Research in Mons is supported by FNRS-FRFC (2Dto3D project - EOS programme) and Région Wallonne (OPTI2MAT excellence programme). The University of Mons and Hasselt University co-authors are grateful for financial support by the Science Policy Office of the Belgian Federal Government (BELSPO; PAI/IAP 7/05). JK is a postdoctoral fellow of the Research Foundation – Flanders (FWO Vlaanderen). NVdB thanks the Vrije Universiteit Brussel for a post-doctoral grant. The HINT COST action MP1202 and French–Irish program ''Hubert Curien Ulysses'' (31998ZF) are also acknowledged for support. This research has also been supported by the European Commission under the 7th Framework Program through the 'Research Infrastructures' action of the 'Capacities' program (contract no: CP-CSA_INFRA-2008-1.1.1

Number 226507-NM13). We further thank the Diamond Light Source for beamtime at the I07 beamline (experiment SI13868) and TA Instruments for the RHC equipment.

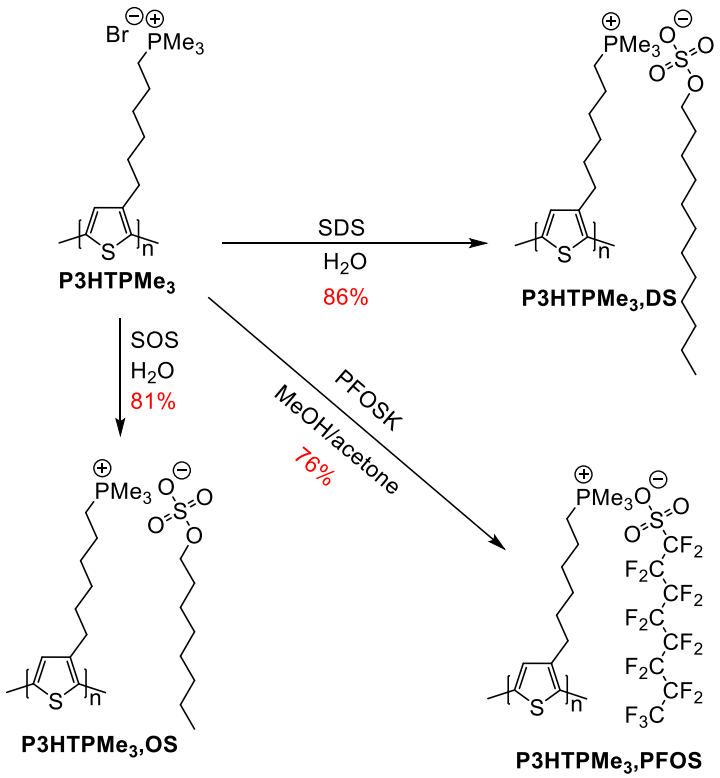

Scheme 1. Conversion of **P3HTPMe3** into the corresponding **P3HTPMe3,X** (X = OS, DS and PFOS) CPEs.

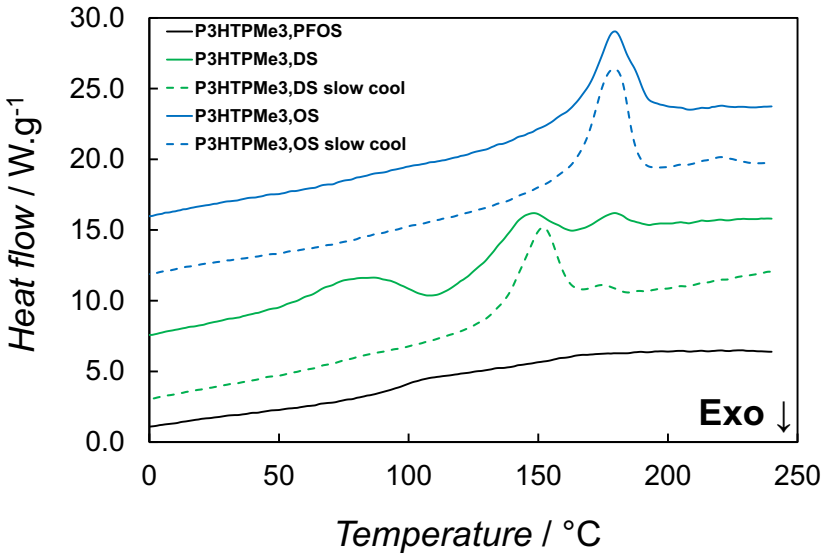

Figure 1. RHC thermograms of the **P3HTPMe3,X** materials at 500 K min^{-1} heating rate, obtained after a previous cooling step at 500 K min^{-1} (solid lines) or 20 K min^{-1} (dashed lines). The curves were shifted vertically for clarity.

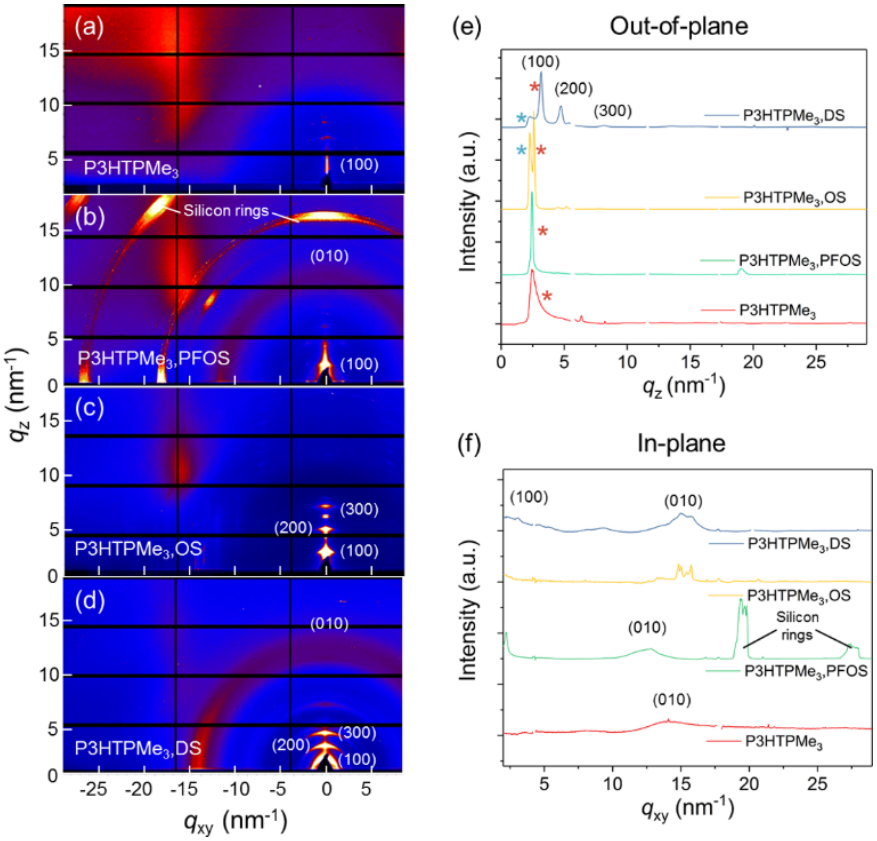

Figure 2. 2D GIWAXS scattering profiles of (a) **P3HTPMe3**, (b) **P3HTPMe3,PFOS**, (c) **P3HTPMe3,OS** and (d) **P3HTPMe3,DS** spin-coated from methanol (10 mg mL^{-1}) onto silicon wafers. Strong intensities in (b) are due to parasitic scattering from the silicon substrate. (e) Out-of-plane and (f) in-plane 1D GIWAXS line profiles corresponding to **P3HTPMe3** (red line), **P3HTPMe3,PFOS** (green line), **P3HTPMe3,OS** (yellow line) and **P3HTPMe3,DS** (blue line). Blue and red stars in (e) serve to highlight the two sets of (100) peaks in the out-of-plane profiles of **P3HTPMe3,OS** and **P3HTPMe3,DS**.

(a)

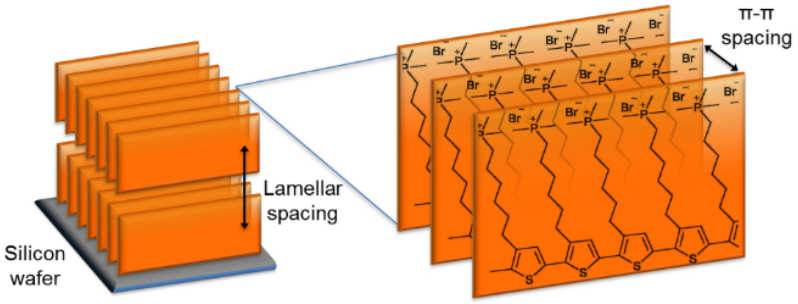

(b)

	Lamellar spacing (nm) [a]	π-π spacing (nm) [a]	Disorder parameter *g* (%) [b]
P3HTPMe$_3$	2.56	0.47	20.0
P3HTPMe$_3$,PFOS	2.51	0.52	18.9
P3HTPMe$_3$,OS	2.42, 2.86*	0.42	19.1
P3HTPMe$_3$,DS	2.51, 2.73*	0.41	13.9

[a] Lamellar and π-π spacings, *d*, were calculated from the position of the (100) and (010) peaks, *q*, respectively, using $d = 2\pi/q$. [b] Disorder parameter, *g*, was estimated using Equation 1. * The second lamellar spacings were determined from the second set of (100) peaks referred to in the text.

Figure 3. (a) Schematic representation of the edge-on alignment of polythiophene chains on a silicon wafer. (b) Table summarizing the structural information for the **P3HTPMe$_3$** and **P3HTPMe$_3$,X** (X = OS, DS, PFOS) CPEs bearing different counterions obtained from GIWAXS studies.

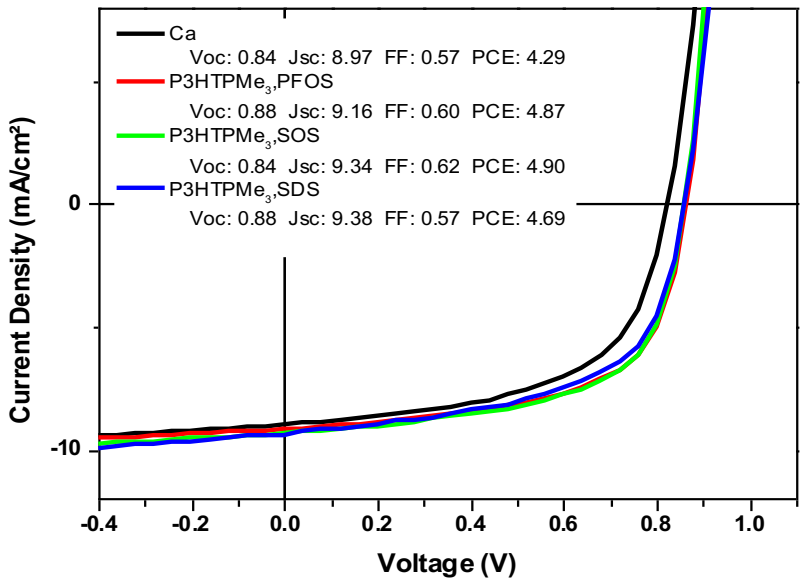

Fig. 4. *J-V* curves for (average efficiency) PCDTBT:PC$_{71}$BM-based BHJ-PSCs employing Ca or CPE interlayers.

Table 1. *J-V* parameters for PCDTBT:$PC_{71}BM$-based BHJ-PSCs employing either Ca or CPE interlayers. The optimal results per concentration for each of the CPEs are indicated in bold.

Interfacial material	Concentration [mg mL^{-1}]	V_{oc} [V]	J_{sc} [mA cm^{-2}]	FF	Average η [%][a)]	Best η [%]
Ca	(30 nm)	0.84	8.61 ± 0.37	0.56	4.08 ± 0.37	4.29
P3HTPMe$_3$,PFOS	0.25	0.84	8.45 ± 0.27	0.59	4.21 ± 0.12	4.32
P3HTPMe$_3$,PFOS	**0.5**	**0.87**	**9.07 ± 0.23**	**0.60**	**4.73 ± 0.11**	**4.98**
P3HTPMe$_3$,PFOS	1	0.85	8.00 ± 0.43	0.36	2.42 ± 0.09	2.58
P3HTPMe$_3$,OS	**0.25**	**0.85**	**9.05 ± 0.33**	**0.61**	**4.70 ± 0.25**	**5.03**
P3HTPMe$_3$,OS	0.5	0.79	8.31 ± 0.41	0.37	2.43 ± 0.23	2.76
P3HTPMe$_3$,DS	0.25	0.86	9.00 ± 0.40	0.60	4.64 ± 0.30	4.96
P3HTPMe$_3$,DS	**0.5**	**0.88**	**9.17 ± 0.32**	**0.59**	**4.75 ± 0.15**	**5.00**
P3HTPMe$_3$,DS	1	0.76	8.94 ± 0.34	0.39	2.68 ± 0.26	3.12

[a)] Average over 4-8 cells.

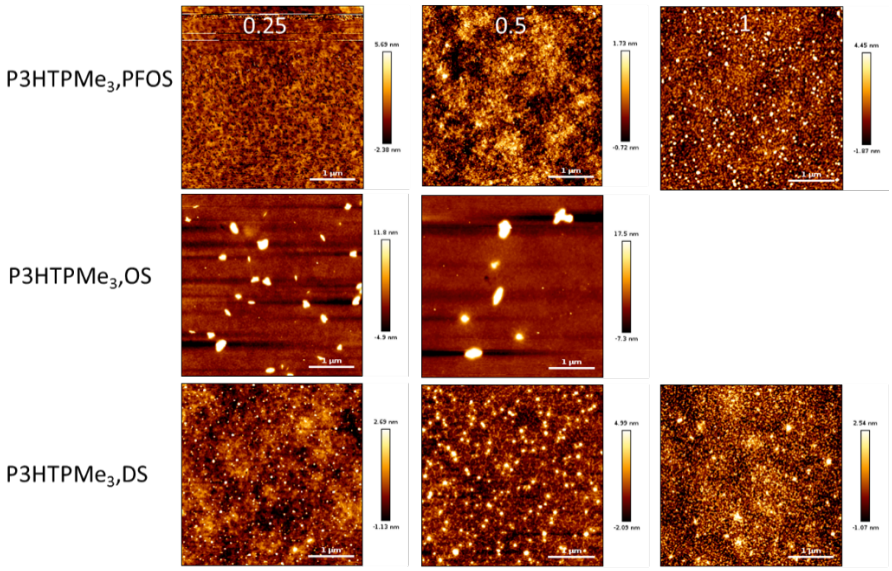

Figure 5. AFM height images (4 × 4 μm^2) of PSCs employing the **P3HTPMe$_3$,X** CPEs with different counterions for different CPE concentrations.

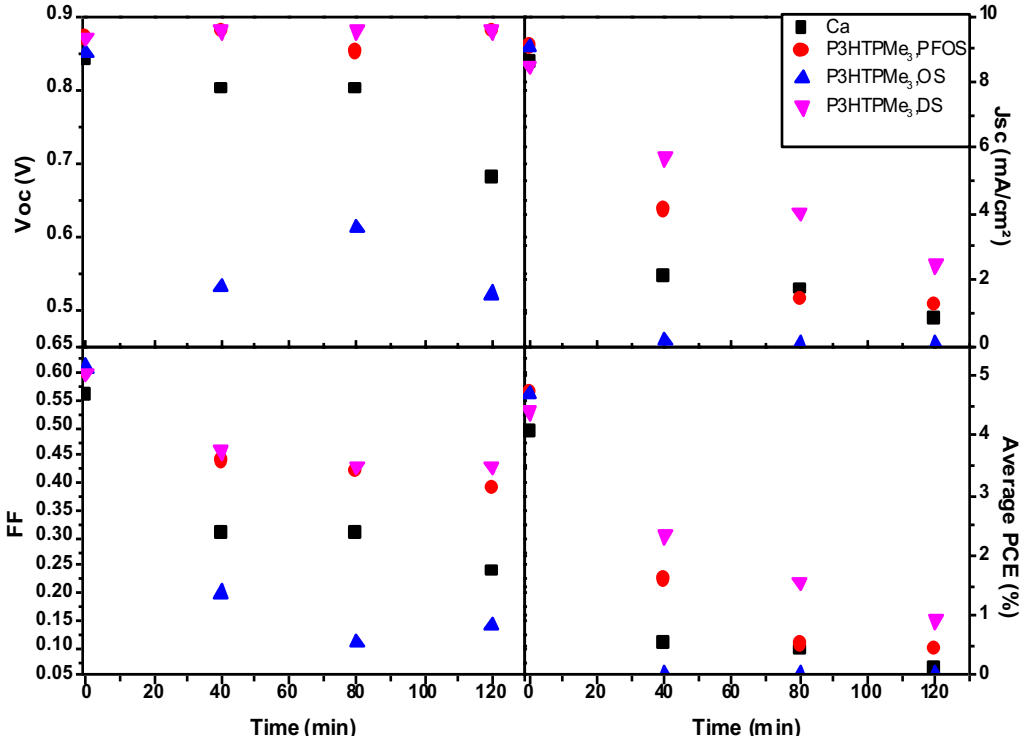

Figure 6. Degradation data (V_{oc}, J_{sc}, FF, average PCE) for PCDTBT:$PC_{71}BM$-based BHJ-PSCs containing either Ca or **P3HTPMe$_3$,X** CPEs as the interfacial layer. The data were recorded in a nitrogen atmosphere after 0, 40, 80 and 120 mins of exposure to air (in the dark).

References

1 H. Jiang, P. Taranekar, J. R. Reynolds and K. S. Schanze, *Angew Chem Int Ed* **48:**4300-4316 (2009).

2 Schanze KS, Zhao X. Structure-Property Relationships and Applications of Conjugated Polyelectrolytes. In: Skotheim TA, Reynolds JR (ed). Handbook of Conducting Polymers, Vol 1, 3rd edn. Boca Raton:CRC Press, 2007; 14-1-14-29

3 Conjugated Polyelectrolytes: Fundamental and Applications , ed by Liu B and Bazan GC. Wiley-VCH, Weinheim (2013).

4 J. Liang, K. Li and B. Liu, *Chem Sci* **4:**1377-1394 (2013).

5 X. Feng, L. Liu, S. Wang and D. Zhu, *Chem Soc Rev* **39:**2411-2419 (2010).

6 S. Das, P. Routh, R. Ghosh, D. P. Chatterjee and A. K. Nandi, *Polymer Int* **66:**623-639 (2017).

7 R. Zhan and B. Liu, *Chem Rec* **16:**1715-1740 (2016).

8 S. Lee, C. H. Jang, T. L. Nguyen, S. H. Kim, K. M. Lee, K. Chang, S. S. Choi, S. K. Kwak, H. Y. Woo and M. H. Song, *Adv Mater* **31:**1900067 (2019).

9 B. R. Lee, J. C. Yu, J. H. Park, S. Lee, C.-K. Mai, B. Zhao, M. S. Wong, E. D. Jung, Y. S. Nam, S. Y. Park, D. Di Nuzzo, J. Y. Kim, S. D. Stranks, G. C. Bazan, H. Choi, M. H. Song and R. H. Friend, *ACS Nano* **12:**5826-5833 (2018).

10 Y. Lee, M. Suh, K. Kim, H. Kim, D. Kim, H. Chang, D. Lee, Y. Kim, S. W. Kim and D. Y. Jeon, *Org Electron* **43:**64-69 (2017).

11 Y. Nishikitani, N. Inokuchi, H. Nishide, S. Uchida, T. Shibanuma and S. Nishimura, *J Phys Chem C* **120:**13976-13986 (2016).

12 W. Lee, J. H. Seo and H. Y. Woo, *Polymer* **54:**5104-5121 (2013).

13 Z. Hu, K. Zhang, F. Huang and Y. Cao, *Chem Commun* **51:**5572-5585 (2015).

14 P. Schmode, D. Ohayon, P. M. Reichstein, A. Savva, S. Inal and M. Thelakkat, *Chem Mater* **31:**5286-5295 (2019).

15 C. Musumeci, M. Vagin, E. Zeglio, L. Ouyang, R. Gabrielsson and O. Inganäs, *J Mater Chem C* **7:**2987-2993 (2019).

16 E. Zeglio, J. Eriksson, R. Gabrielsson, N. Solin and O. Inganäs, *Adv Mater* **29:**1605787 (2017).

17 E. Zeglio, M. M. Schmidt, M. Thelakkat, R. Gabrielsson, N. Solin and O. Inganäs, *Chem Mater* **29:**4293-4300 (2017).

18 E. Zeglio, M. Vagin, C. Musumeci, F. N. Ajjan, R. Gabrielsson, X. T. Trinh, N. T. Son, A. Maziz, N. Solin and O. Inganäs, *Chem Mater* **27:**6385-6393 (2015).

19 J. E. Houston, S. Richeter, S. Clément and R. C. Evans, *Polym Int* 1333-1348 (2017).

20 Z. He, H. Wu and Y. Cao, *Adv Mater* **26:**1006-1024 (2014).

21 M. Chevrier, J. E. Houston, J. Kesters, N. Van den Brande, A. E. Terry, S. Richeter, A. Mehdi, O. Coulembier, P. Dubois, R. Lazzaroni, B. Van Mele, W. Maes, R. C. Evans and S. Clement, *J Mater Chem A* **3:**23905-23916 (2015).

22 J. H. Seo, R. Yang, J. Z. Brzezinski, B. Walker, G. C. Bazan and T.-Q. Nguyen, *Adv Mater* **21:**1006-1011 (2009).

23 S. van Reenen, S. Kouijzer, R. A. J. Janssen, M. M. Wienk and M. Kemerink, *Adv Mater Interfaces* **1:**1400189 (2014).

24 M. Y. Jo, Y. E. Ha, Y. S. Won, S. I. Yoo and J. H. Kim, *Org Electron* **25:**85-91 (2015).

25 J. Drijkoningen, J. Kesters, T. Vangerven, E. Bourgeois, L. Lutsen, D. Vanderzande, W. Maes, J. D'Haen and J. Manca, *Org Electron* **15:**1282-1289 (2014).

26 T. P. Voortman and R. C. Chiechi, *ACS Appl Mater Interfaces* **7:**28006-28012 (2015).

27 J. E. Houston, M. Chevrier, M.-S. Appavou, S. M. King, S. Clément and R. C. Evans, *Nanoscale* **9:**17481-17493 (2017).

28 P. A. Korevaar, T. F. A. de Greef and E. W. Meijer, *Chem Mater* **26:**576-586 (2014).

29 R. Noriega, J. Rivnay, K. Vandewal, F. P. V. Koch, N. Stingelin, P. Smith, M. F. Toney and A. Salleo, *Nat Mater* **12:**1038-1044 (2013).

30 L. Ying, F. Huang and G. C. Bazan, *Nat Commun* **8:**14047 (2017).

31 G. Hostnik, Č. Podlipnik, G. Mériguet and J. Cerar, *Macromolecules* **53:**1119-1128 (2020).

32 R. Yang, A. Garcia, D. Korystov, A. Mikhailovsky, G. C. Bazan and T.-Q. Nguyen, *J Am Chem Soc* **128:**16532-16539 (2006).

33 G. Hostnik, M. Bončina, C. Dolce, G. Mériguet, A.-L. Rollet and J. Cerar, *Phys Chem Chem Phys* **18:**25036-25047 (2016).

34 R. D. McCullough, P. C. Ewbank and R. S. Loewe, *J Am Chem Soc* **119:**633-634 (1997).

35 Z. Chen, Z. Hu, Z. Wu, X. Liu, Y. Jin, M. Xiao, F. Huang and Y. Cao, *J Mater Chem A* **5:**19447-19455 (2017).

36 C. D. Danesh, N. S. Starkweather and S. Zhang, *J Phys Chem B* **116:**12887-12894 (2012).

37 H. D. Burrows, M. J. Tapia, C. L. Silva, A. A. C. C. Pais, S. M. Fonseca, J. Pina, J. Seixas de Melo, Y. Wang, E. F. Marques, M. Knaapila, A. P. Monkman, V. M. Garamus, S. Pradhan and U. Scherf, *J Phys Chem B* **111:**4401-4410 (2007).

38 L. Chen, S. Xu, D. McBranch and D. Whitten, *J Am Chem Soc* **122:**9302-9303 (2000).

39 R. C. Evans, M. Knaapila, N. Willis-Fox, M. Kraft, A. Terry, H. D. Burrows and U. Scherf, *Langmuir* **28:**12348-12356 (2012).

40 M. Knaapila, R. C. Evans, V. M. Garamus, L. Almásy, N. K. Székely, A. Gutacker, U. Scherf and H. D. Burrows, *Langmuir* **26:**15634-15643 (2010).

41 M. Knaapila, R. C. Evans, A. Gutacker, V. M. Garamus, N. K. Székely, U. Scherf and H. D. Burrows, *Soft Matter* **7:**6863-6872 (2011).

42 Y.-M. Chang, R. Zhu, E. Richard, C.-C. Chen, G. Li and Y. Yang, *Adv Funct Mater* **22:**3284-3289 (2012).

43 A. Garcia, Y. Jin, J. Z. Brzezinski and T.-Q. Nguyen, *J Phys Chem C* **114:**22309-22315 (2010).

44 M. M. Schmidt, M. ElMahmoudy, G. G. Malliaras, S. Inal and M. Thelakkat, *Macromol Chem Phys* **219:**1700374 (2018).

45 A. Garcia, J. Z. Brzezinski and T.-Q. Nguyen, *J Phys Chem C* **113:**2950-2954 (2009).

46 T. T. Do, H. S. Hong, Y. E. Ha, J. Park, Y.-C. Kang and J. H. Kim, *ACS Appl Mater Interfaces* **7:**3335-3341 (2015).

47 J. Kesters, S. Govaerts, G. Pirotte, J. Drijkoningen, M. Chevrier, N. Van den Brande, X. Liu, M. Fahlman, B. Van Mele, L. Lutsen, D. Vanderzande, J. Manca, S. Clément, E. Von Hauff and W. Maes, *ACS Appl Mater Interfaces* **8:**6309-6314 (2016).

48 J. H. Seo, A. Gutacker, Y. Sun, H. Wu, F. Huang, Y. Cao, U. Scherf, A. J. Heeger and G. C. Bazan, *J Am Chem Soc* **133:**8416-8419 (2011).

49 J. Kesters, T. Ghoos, H. Penxten, J. Drijkoningen, T. Vangerven, D. M. Lyons, B. Verreet, T. Aernouts, L. Lutsen, D. Vanderzande, J. Manca and W. Maes, *Adv Energy Mater* **3:**1180-1185 (2013).

50 J. Rubio-Magnieto, A. Thomas, S. Richeter, A. Mehdi, P. Dubois, R. Lazzaroni, S. Clement and M. Surin, *Chem Commun* **49:**5483-5485 (2013).

51 J. H. Scofield, *J Electron Spectrosc Relat Phenom* **8:**129-137 (1976).

52 S. Wouters, F. Demir, L. Beenaerts and G. Van Assche, *Thermochim Acta* **530:**64-72 (2012).

53 Bard AJ, Faulker LR, in Electrochemical Methods: Fundamentals and Applications, John Wiley and Sons, New York, 2nd edn, 2001

54 S. Trasatti, *Pure Appl Chem* **58:**955-966 (1986).

55 R. L. Danley, P. A. Caulfield and S. R. Aubuchon, *Am Lab* **40:**9-11 (2008).

56 C. Nicklin, T. Arnold, J. Rawle and A. Warne, *J Synchrotron Rad* **23:**1245-1253 (2016).

57 M. Basham, J. Filik, M. T. Wharmby, P. C. Y. Chang, B. El Kassaby, M. Gerring, J. Aishima, K. Levik, B. C. A. Pulford, I. Sikharulidze, D. Sneddon, M. Webber, S. S. Dhesi, F. Maccherozzi, O. Svensson, S. Brockhauser, G. Naray and A. W. Ashton, *J Synchrotron Rad* **22:**853-858 (2015).

58 J. Rivnay, S. C. B. Mannsfeld, C. E. Miller, A. Salleo and M. F. Toney, *Chem Rev* **112:**5488-5519 (2012).

59 H. Sirringhaus, P. J. Brown, R. H. Friend, M. M. Nielsen, K. Bechgaard, B. M. W. Langeveld-Voss, A. J. H. Spiering, R. A. J. Janssen, E. W. Meijer, P. Herwig and D. M. de Leeuw, *Nature* **401:**685-688 (1999).

60 T.-A. Chen, X. Wu and R. D. Rieke, *J Am Chem Soc* **117:**233-244 (1995).

61 A. M. Hindeleh and R. Hosemann, *J Phys C* **21:**4155 (1988).

62 J. Guo, Y. Liang, J. Szarko, B. Lee, H. J. Son, B. S. Rolczynski, L. Yu and L. X. Chen, *J Phys Chem B* **114:**742-748 (2010).

63 J. Jung, W. Lee, C. Lee, H. Ahn and B. J. Kim, *Adv Energy Mater* **6:**1600504 (2016).

64 T. Lei, J.-H. Dou and J. Pei, *Adv Mater* **24:**6457-6461 (2012).

65 T. L. Nguyen, H. Choi, S. J. Ko, M. A. Uddin, B. Walker, S. Yum, J. E. Jeong, M. H. Yun, T. J. Shin, S. Hwang, J. Y. Kim and H. Y. Woo, *Energy Environ Sci* **7:**3040-3051 (2014).

66 Y. D. Park, H. S. Lee, Y. J. Choi, D. Kwak, J. H. Cho, S. Lee and K. Cho, *Adv Funct Mater* **19:**1200-1206 (2009).

67 B. J. Kim, Y. Miyamoto, B. Ma and J. M. J. Fréchet, *Adv Funct Mater* **19:**2273-2281 (2009).

68 Y. Zhou, C. Fuentes-Hernandez, J. Shim, J. Meyer, A. J. Giordano, H. Li, P. Winget, T. Papadopoulos, H. Cheun, J. Kim, M. Fenoll, A. Dindar, W. Haske, E. Najafabadi, T. M. Khan, H. Sojoudi, S. Barlow, S. Graham, J.-L. Brédas, S. R. Marder, A. Kahn and B. Kippelen, *Science* **336:**327-332 (2012).

69 Z. Hu, N. Zheng, S. Dong, X. Liu, Z. Chen, L. Ying, C. Duan, F. Huang and Y. Cao, *Org Electron* **57:**151-157 (2018).

70 K. Zhang, C. Zhong, S. Liu, C. Mu, Z. Li, H. Yan, F. Huang and Y. Cao, *ACS Appl Mater Interfaces* **6:**10429-10435 (2014).

71 S. Govaerts, J. Kesters, M. Defour, B. Van Mele, H. Penxten, S. Neupane, F. U. Renner, L. Lutsen, D. Vanderzande and W. Maes, *Eur Polym J* **97:**49-56 (2017).

72 M. Jørgensen, K. Norrman and F. C. Krebs, *Sol Energ Mat Sol Cells* **92:**686-714 (2008).